

# Annual variability in a conceptual climate model: Snapshot attractors, hysteresis in extreme events, and climate sensitivity

Tamás Bódai<sup>1,2</sup> and Tamás Tél<sup>2</sup>

<sup>1</sup>Max Planck Institute for the Physics of Complex Systems, Nöthnitzer St. 38, 01187 Dresden, Germany

<sup>2</sup>Institute for Theoretical Physics–HAS Research Group, Eötvös University, Pázmány P. s. 1/A, Budapest, H–1117, Hungary

(Received 20 October 2011; accepted 5 March 2012; published online 17 April 2012)

In a conceptual model of global atmospheric circulation, the effects of annually periodic driving are investigated. The driven system is represented in terms of snapshot attractors, which may remain fractal at all times. This is due to the transiently chaotic behavior in the regular parameter regimes of the undriven system. The driving with annual periodicity is found to be relatively fast: There is a considerable deviation from the undriven case. Accordingly, the existence of a hysteresis loop is identified, namely, the extremal values of a given variable depend not only on the actual strength of the insolation but also on the sign of its temporal change. This hysteresis is due to a kind of internal memory. In the threshold-dependence of mean return times of various extreme events, a roughly exponential scaling is found. Climate sensitivity parameters are defined, and the measure of certain types of extremal behavior is found to be strongly susceptible to changes in insolation. © 2012 American Institute of Physics. [<http://dx.doi.org/10.1063/1.3697984>]

**Conceptual climate models play a special role, since they are well suited as testing grounds for different theoretical ideas. The concept of snapshot attractors<sup>1</sup> (or, equivalently, that of the more recently coined pullback attractors<sup>2</sup>) of dynamical systems has been suggested<sup>3,4</sup> as a promising tool to describe the variance of climate, due to uncertainties in the parameters, in a novel way. To this end, one should investigate an ensemble of trajectories, all subject to the same realization of noise. After some time, the ensemble traces out a snapshot attractor and also determines a distribution on it. The attractor is changing continuously in time. In general, a snapshot attractor of a driven system is an object which attracts any trajectories initialized in the infinitely remote past within a basin of attraction.<sup>3</sup> A snapshot attractor can be either a simple object or a fractal. Here, we show that the concept of snapshot attractors can usefully be applied to higher dimensional systems with strictly time-periodic driving, too.**

humidity, atmospheric pressure, wind, rainfall, etc. But, climate can also be defined as “the statistical properties of the state of the atmosphere-ocean system, taken over an ensemble of appropriate initial conditions.”<sup>15</sup> Note that this ensemble is exactly what is represented by a snapshot attractor.

Therefore, *climate change can be seen as the evolution of snapshot attractors*. From a different point of view, we can say that the climate is sensitive if under slightly different conditions, the climate snapshot attractor takes substantially different shapes.

In particular, we will consider measures of the climate snapshot attractor in association with extremal behavior. A key parameter that determines the state of the climate is the strength of solar radiation, or solar forcing, called insolation in brief. We also investigate climate sensitivity, or the susceptibility of the climate, to change the amplitude and the mean value of the insolation.

Extreme events have already been studied in elementary chaotic models.<sup>16,17</sup> In our periodically driven model climate, we study extreme events and their return time statistics as a function of the threshold level.

Extremes are also studied in terms of the extremal values of variables. We find a continuous annual variation of the extremal values and a hysteresis loop in it. Hysteresis in a different climatic situation has been found recently in averaged quantities by Bordi *et al.*,<sup>18</sup> e.g., in the transient response of the mean surface temperature to the changing of well-mixed green house gases.

The paper is organized as follows. Next, in Sec. II, the model is introduced and explained. In Sec. III, snapshot attractors are determined. Two-dimensional snapshot attractors are equivalent in this periodically driven case to slices of a three-dimensional stroboscopic map. After investigating the bifurcation diagram (Sec. IV), extreme events are studied; first, a memory hysteresis in the sense of Ref. 18 is identified (Sec. V A), and then extreme event return time

## I. INTRODUCTION

As a conceptual model, we consider Lorenz’s model of global atmospheric circulation (L84)<sup>5</sup> with a driving of annual periodicity.<sup>6</sup> This low-order model is not only appealing,<sup>7–14</sup> but it can be derived from the quasi-geostrophic equations governing the large-scale motion of the atmosphere.<sup>6,8</sup>

As an early attempt to study the long-term variability in Lorenz’s model with annual periodicity, Pielke and Zheng<sup>7</sup> evaluated the power spectrum of various long model time series. Here, we shall focus on extreme event return time statistics, climate sensitivity, and overall variability in view of snapshot attractors.

Climate is commonly defined as a makeup of long-time averages of meteorological measurements, e.g., temperature,

statistics are presented (Sec. V B). In Sec. VI, we discuss the issue of climate sensitivity and point out a basic difference between sensitivity in the summer and winter periods. In Sec. VII, we draw conclusions. A description and classification of numerical sectioning techniques to create snapshot attractors can be found in the Appendix.

## II. MODEL

The model to be studied reads as follows:<sup>6</sup>

$$\begin{aligned} \dot{x} &= -y^2 - z^2 - ax + aF(t), \\ \dot{y} &= xy - bxz - y + 1, \\ \dot{z} &= xz + bxy - z; \end{aligned} \quad (\text{L84})$$

where  $F(t)$  is a time-periodic driving:

$$F(t) = F_0 + A \sin(\omega t). \quad (1)$$

The physical content of L84 is that the solar forcing, represented by  $F$ , creates a temperature difference between the equator and the pole, which, via geostrophic balance, influences most directly the wind speed of the Westerlies represented by  $x$ . As an effect of baroclinic instability, cyclonic activity facilitates poleward heat transport, two modes of which are represented by  $y$  and  $z$ .

For the parameter setting, we take the common choice:  $a = 1/4$  and  $b = 4$ .<sup>5</sup> The equations appear in a dimensionless form with the time unit corresponding to about 5 days. The constant value of  $F(t) = F_0 = 6$  (8) was regarded by Lorenz to be an appropriate value for permanent summer (winter), and the system with this value exhibits only periodic (chaotic) attractors.

The periodic forcing (1) taken about the mean value  $F_0 = 7$  (Ref. 6) describes the variation of the insolated energy over a year. Since one year is about  $T = 73$  time units, we set  $\omega = 2\pi/73$ . Note that time  $t \bmod T = 0$  in expression (1) coincides with the September equinox. Midwinters and midsummers correspond to  $t \bmod T = T/4 = 18.25$  and  $3T/4 = 54.75$ , respectively. As for the physical origin of the forcing, we note that  $F(t)$  may also contain—in association with the greenhouse effect—the contribution of the varying  $\text{CO}_2$  content.

The coupling amplitude  $A$  is set in the main body of the paper to  $A = 2$ , the same value that Lorenz used in Ref. 6, but for comparison, in Sec. VII we shall also consider other values of  $A$  down to  $A = 1$ , in which latter case the extrema of  $F(t)$  correspond to the Lorenzian winter and summer.

Figure 1 shows the time series of variable  $x$  over four subsequent years. The most striking feature, also observed by Lorenz,<sup>6</sup> is that active and inactive summers follow each other in a random sequence (the former occurring about four times as often as the latter, as a longer simulation would show), while the subsequent chaotic winters are not very different. This interannual variability was interpreted as a consequence of the fact that by the periodic forcing, the two coexisting periodic attractors (a period-1 and a period-4 cycle) of a permanent summer with  $F = 6$  are coupled in a chaotic or random manner.<sup>10</sup>

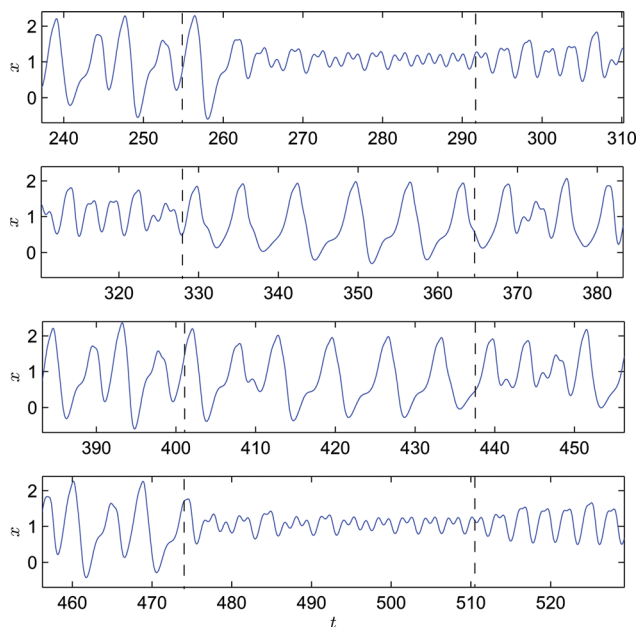


FIG. 1. Time evolution of the  $x$  component of the L84 system with annually periodic driving, over four years following consecutively in four panels ( $F_0 = 7$  and  $A = 2$ ). The first time instant shown corresponds to 237.25 time units (3.25 years), which is much longer than the dissipative relaxation time, found to be about 30 time units. The time interval of each panel ranges from midwinter to midwinter. Vertical dashed lines mark the March and September equinoxes. Winters are always chaotic, and more regular active and inactive summers follow each other in a random manner.

It has long been thought that a simple representation of the full chaotic attractor is hopeless, since even the stroboscopic map (taken on a preselected day of the year) has a three-dimensional chaotic attractor and is, therefore, difficult to visualize. We show in what follows that snapshot attractors, or equivalent realizations of them, provide a useful tool for a two-dimensional visualization of the climatic attractor.

## III. SNAPSHOT ATTRACTORS

Stochastically or chaotically driven dissipative systems of three variables possess three dimensional snapshot attractors.<sup>3,4,14</sup> They are obtained by considering the instantaneous coordinates of an ensemble of trajectories, followed from a smooth distribution at time  $t_0 = 0$  up to a certain time  $t \gg 1$ , all trajectories subject to the same realization of noise or chaotic driving. Intersections of these 3D snapshot attractors with a surface, i.e., 2D snapshot attractors, are the generalizations of attractors appearing on Poincaré surfaces of intersection of autonomous systems with three-dimensional phase spaces. Most typically, the attractor is chaotic whose fractal pattern is changing continuously in time.<sup>14</sup>

The concept of snapshot attractors has been known for many years.<sup>1,19–21</sup> Here, we extend the concept to a system with periodic driving.

In the L84 model, the traditional Poincaré surface is the plane  $z = 0$  with  $\dot{z} > 0$ ,<sup>5</sup> and we restrict ourselves to this traditional choice. In three-variable systems driven periodically in time with period  $T$ , there exists, at any phase of the period, a unique three-dimensional stroboscopic attractor that can be

defined by a single long trajectory. Since, due to ergodicity, this attractor can also be generated by an ensemble of trajectories started in the remote past and stopped at some time  $t$ , the stroboscopic attractor can, in this special case, also be considered as a 3D snapshot attractor. The  $z=0$  section of this attractor is a 2D snapshot attractor with coordinates  $x, y$ . Numerically, we found it even more convenient to consider a single long trajectory, store its  $x, y$  coordinates, and the time when  $z=0$ , and select afterwards all data points that belong to time  $t \bmod T$ . Note that due to the periodicity of the driving, the evolving snapshot attractor indeed repeats itself after  $T=73$  time units. The results can be seen in Fig. 2. In the particular  $z=0$  Poincaré section any pair of  $(x, y)$  coordinates are either both positive or both negative, which can be easily explained in terms of the third equation of L84. In the examples presented in Fig. 2, snapshot attractors live in the first quadrant of the plane. Numerical techniques by which snapshots can be constructed are presented and discussed in the Appendix.

The most striking feature is the very large variability. The largest  $x$  and  $y$  values and their occurrence probability changes drastically with time. The accumulation of points in a summer plot [Fig. 2(d)] in the middle of the picture and in four strongly localized regions correspond to the observation by the time series of Fig. 1 that summers are characterized by nearly period-1 and period-4 cycles.

One might think that a driving whose period is nearly 100 times that of the basic time unit is so slow that the driven system is simply scanning through the states corresponding to the attractors of the undriven problem. Snapshots in Fig. 2 are taken at two pairs of time instants when the driving, either increasing ( $\dot{F} > 0$ ) or decreasing ( $\dot{F} < 0$ ), hits the value of  $F=8$  [Figs. 2(a) and 2(b)] or  $F=6$  [Figs. 2(c) and 2(d)]. If the above conjecture was true, the two attractors with

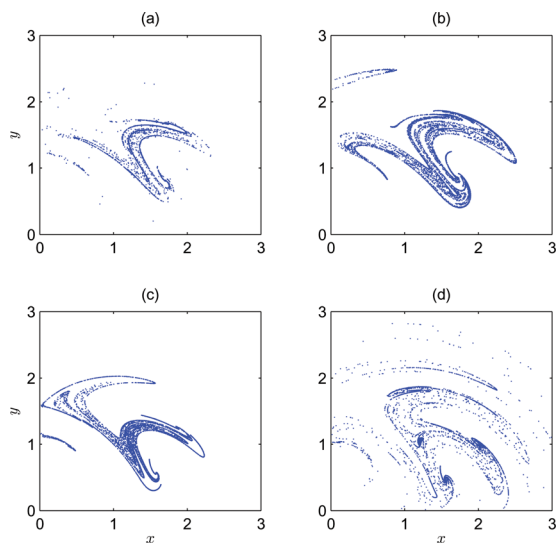


FIG. 2. The  $z=0$  Poincaré sections of snapshot attractors at chosen times of the year, associated with (a)  $t=T/12$ ,  $F(t)=8$ , (b)  $t=5T/12$ ,  $F(t)=8$ , (c)  $t=7T/12$ ,  $F(t)=6$ , and (d)  $t=11T/12$ ,  $F(t)=6$ . Each of the snapshots is constituted by  $N=10^4$  intersection points. A number of almost  $2 \times 10^3$  such snapshots have been constructed over a period of one year, which facilitate the creation of a sufficiently smooth movie of the evolution of the 2D snapshot attractor (enhanced online). [URL: <http://dx.doi.org/10.1063/1.3697984.1>]

$F=8$  (or  $F=6$ ) should be identical. Their strong difference (and also the nonexistence of an exact stroboscopic fixed point and period-4 attractors during summer) shows that the annual driving is still fast enough to make the dynamics much richer than without driving.

A point of interest is that none of the snapshot attractors is regular—not only the examples displayed in Fig. 2 but none throughout the period of a year, as shown in the movie of the supplementary material.<sup>22</sup> This is interesting in view of the extended periodic windows appearing in the bifurcation diagram in the range  $5 \leq F \leq 9$  that the value of  $F(t)$  scans. For a better understanding of this, details of the bifurcation diagram in Fig. 3, and its construction will be discussed next.

#### IV. BIFURCATION DIAGRAM

A bifurcation diagram, by definition, represents attractor-type solutions only. However, a picture of transient behavior can give further insight. Such a picture can be obtained by using an ensemble of trajectories, too.

When long chaotic transients are present, the straightforward construction of the bifurcation diagram may be difficult. In the following, three stages of constructing the bifurcation diagram are described, in the first stage, conveniently, obtaining a picture of chaotic transients.

Fig. 3(a) was constructed by using an ensemble of  $N=10^4$  trajectories, randomly initialized in  $0 < (x, y) < 2$  with  $z=0$  for each fixed value of  $F$ , with which it is anticipated that most of the coexisting attractors can be found. The ensemble is followed up to 20 iterations on the  $z=0$  Poincaré

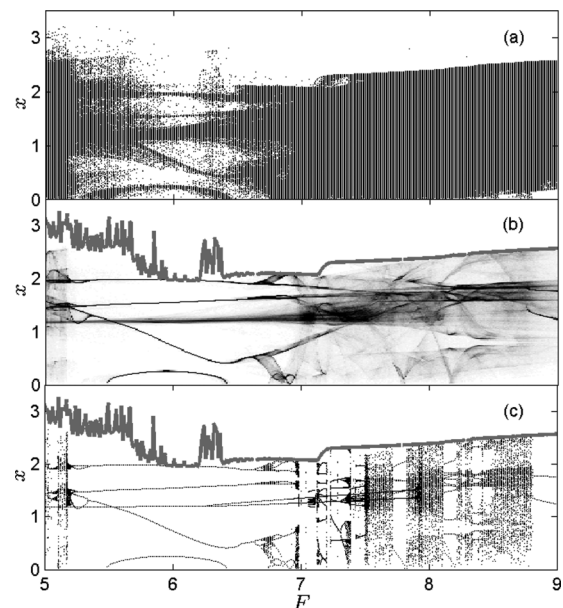


FIG. 3. Bifurcation diagram and preliminary stages of its construction. (a) “Extended” bifurcation diagram containing signs of transient chaos as well:  $x$  vs  $F$  obtained from the 20 times iterated Poincaré maps of ensembles of trajectories. (b) The density of the ensemble along the  $x$  axis is indicated by gray scale colors, with lighter shades for smaller densities. White (black) corresponds to a density of zero ( $\geq 300$  points) in a bin of the histogram. (c) Bifurcation diagram,  $x$  vs  $F$ , using several long trajectories. All coexisting attractors are represented.

surface, and finally, the  $x$  coordinates of trajectory endpoints are plotted only. This method leaves some long chaotic transients and permanently chaotic motions undistinguishable. Since by iteration 20, many trajectories have not yet left the chaotic saddles underlying transient chaos, this diagram can be considered as an approximant to an “extended” bifurcation diagram containing all chaotic sets (i.e., attractors and saddles) and the periodic points.

Some points approach certain attractors faster than some others. Therefore, when simulating the time evolution of an ensemble up to a finite time (20 Poincaré steps in our case), the projection of the ensemble onto the  $x$ -axis is inhomogeneous. The density in this distribution is gray coded in Fig. 3(b). A density larger than a threshold value, e.g., 150 points/bin, can identify permanent structures, such as periodic cycles. Points that contribute to much smaller densities exhibit transient chaos.

In order to proceed with the construction of the commonly defined bifurcation diagram in the third stage, a large ensemble would be very expensive to simulate further on, and instead the structures present after 20 iterations are sampled. To this end, the threshold density of a two-dimensional distribution of the ensemble over the  $x$ - $y$  plane (200 bins in  $x_{min} < x < x_{max}$  and  $y_{min} < y < y_{max}$ ) is set to 20 points/bin, and from each bin one point is randomly selected for an additional simulation of over 1000 dimensionless time units, and the last 100 points of intersection with the Poincaré surface are plotted. Ten other initial conditions are also chosen randomly to capture possibly coexisting chaotic attractors. Once periodic cycles are identified, it is investigated how far they extend in terms of  $F$ , by following the attractor, with an increment of  $\Delta F = 0.002$ . This procedure resulted in the bifurcation diagram shown in Fig. 3(c). In this, and also in the diagram of the distribution in panel (b), a solid gray curve indicates the maximal  $x$  coordinates for each value of  $F$ , as can be seen in the diagram in panel (a).

We have found that transient chaos is indeed present in the whole span of  $F \in [5, 9]$ . Most of the time, it is due to the coexistence of periodic attractors and so the existence of a basin boundary and the associated chaotic saddle. One such saddle (red) with its stable (blue) and unstable (green) manifolds is displayed in Fig. 4. It is found for  $F = 6$ , when a period-four and a period-one cycle coexist (indicated by markers). The saddle lies at the intersection of its stable and unstable manifolds.<sup>23,24</sup> The latter manifold resembles the snapshot attractor at  $t = 11T/12$ ,  $F(t) = 6$ , as in Fig. 2(d). That is, a fractal snapshot attractor of the driven system is similar to the unstable manifold of the chaotic saddles of the undriven system, which is populated by escaping trajectories approaching periodic cycles. The fact that none of the snapshot attractors is completely regular is due to the finite time scales of escape and a relatively fast driving.

For other fixed values of  $F$ , other periodic cycles might coexist, which imply nonattracting chaotic objects similar to the saddle in Fig. 4. The regime of coexisting period-one and period-four cycles discovered by Lorenz span a wide range, about  $[5.3, 6.7]$ , before period-doubling cascades take place at both ends, which end up in chaos. In the range of about  $[5.5, 2]$ , different regimes change each other, when transient

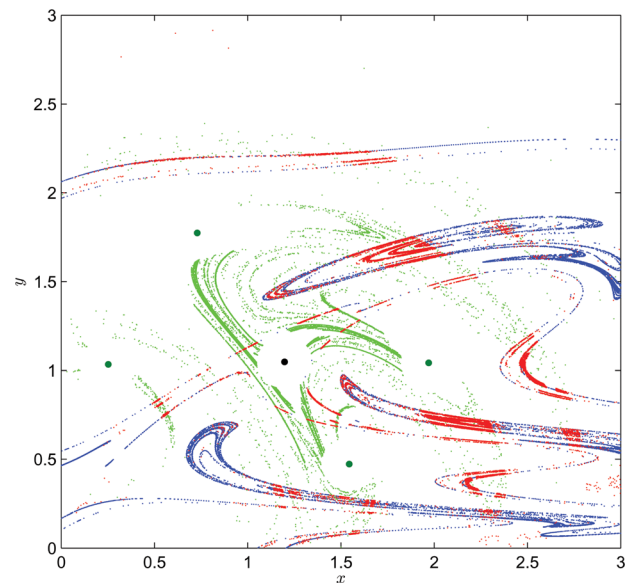


FIG. 4. Chaotic saddle (red) and its stable (blue) and unstable (green) manifolds on the  $z=0$  Poincaré surface for  $F=6$ , represented by over  $2 \times 10^4$  points. For the construction of these, a trajectory is regarded to have escaped from near the saddle, if it approached one of the periodic points (large dots) with a separation less than  $\varepsilon = 0.15$  (blank circles around the periodic points). Initially, an ensemble of  $32^2 \cdot 100^2 > 10^7$  points is taken on a rectangular array in the region shown. The unstable (stable) manifold is approximated by the endpoints (initial points) of trajectories which have not escaped up to 18 iterations, and the saddle, as the intersection (set) of its stable and unstable manifolds, is approximated by the midpoints of the nonescaped trajectories (at iteration number 9).<sup>12,25</sup>

chaos is due most of the time to coexistence of periodic attractors again, or sometimes, as an interesting effect,<sup>25</sup> transient chaos occurs without coexistence of attractors, as also noted in Ref. 11. The case of  $F=5$  is an example for the latter, and it happens to be the case that the transient is very long—longer than the time span of simulation (1000 time units). After the period-doubling cascade just before  $F=7$ , permanent chaos ceases to exist abruptly via a crisis. In the forthcoming range, up to about  $F=7.5$ , a period-two cycle either coexists with one [(e.g.,  $F=7.3$ ) or more (e.g.,  $F=7.45$ )] higher-period cycles, or exists on its own. Beyond this, it coexists with permanent chaos (e.g.,  $F=7.6, 7.9$ ). The Lorenzian chaotic winter attractor at  $F=8$  is again a single global attractor. The bifurcation diagram of Fig. 3(c) provides much more detail than the one sketched by Lorenz in Ref. 6, in particular, it illustrates the abundance of periodic windows.

## V. EXTREME VALUE STATISTICS

### A. Hysteresis in extreme values

When a process produces a stationary distribution, extreme value statistics is concerned with the tail of this distribution. In our model, in any phase of the year, such a stationary distribution is well defined, with a finite maximum of its domain.<sup>26</sup>

Over the period of a year, these maxima create an envelope curve of the 3D snapshot attractors projected on any axis. For convenience, we can also consider the  $z=0$  section, i.e., the 2D snapshot attractors, as shown in Fig. 2 (see also

corresponding movie file). These envelopes are called *dynamic* envelopes, in contrast with the set of maximal  $x$  coordinates of the undriven system shown in Fig. 3, which we refer to as *static* envelope.

The dynamic envelopes in the  $x$  and  $y$  directions of the 3D attractors [thin gray lines in Figs. 5(a) and 5(b), respectively] are obtained by an ensemble of  $10^7$  trajectories. The resolution of these curves in time is the same as the step size of integration, 0.005 time units. These envelopes are thus numerically approximated, and resolved in time, very accurately.

The dynamic envelopes in the  $x$  and  $y$  directions of the 2D snapshot attractor [thick black lines in Figs. 5(a) and 5(b), respectively] are obtained—because of the constraint corresponding to  $z=0$ —with only  $10^4$  points. These envelopes exhibit larger fluctuations than the 3D envelopes, since they are generated based on a smaller number of points. The envelope is the more likely to appear as a fluctuating curve using an ensemble of a fixed number of points, the less frequent are the associated extremes, i.e., the thinner is the tail of the distribution over the snapshot attractor. For reference, we provide examples of snapshot distributions, which are obtained by projecting the 3D snapshot attractors onto the  $y$  axis. Fig. 6 shows such distributions corresponding to the instants of snapshots in Fig. 2. As can be seen in panels (a) and (d) of these two figures, corresponding to the upper branch of the  $y$  envelopes, long and thin tails of the distributions and a few widely scattered points in the Poincaré sections, respectively, describe rather rare extremes. On the contrary, in panels (b) and (c) of the said two figures, corre-

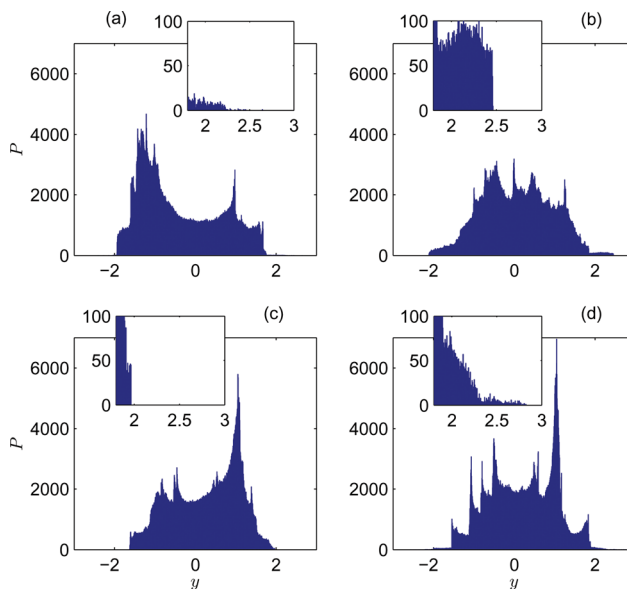


FIG. 6. Histograms by the projection of 3D snapshot attractors onto the  $y$  axis at instants corresponding to snapshots in Fig. 2. The insets display magnified views of the tails of the maxima.

sponding to the lower branch of the  $y$  envelopes, short and bulky tails of the distributions and sharp edges of the 2D snapshot attractors, respectively, describe more frequent extremes. These figures, thus, indicate that the extreme value statistics, and, consequently, the size of the fluctuations of the envelopes is strongly season- or  $F$ -dependent: The curves are fairly jagged/smooth for the increasing/decreasing branches. For comparison, the curves of maximal  $x$  and  $y$  coordinate in the bifurcation diagrams [as seen in Fig. 3(c) for  $x$ ], i.e., the static envelopes, are also shown in Fig. 5 with thick gray lines.<sup>27</sup>

A basic observation with regard to the dynamic envelopes is that they feature a *hysteresis loop*, i.e., they exhibit separate branches when  $F$  increases or decreases. Note that the static envelope is by definition without any hysteresis.

Let us compare the static envelopes with the dynamic envelopes of the 2D snapshot attractors. The mere presence of the hysteresis in the dynamic one indicates a strong difference between the driven and the undriven systems. The deviation appears to be most pronounced for  $F > 5.8$  for  $F$  increasing. For decreasing  $F$ , the dynamic and static envelopes happen to be rather close to each other for  $F > 7.3$ .

An interesting feature can be extracted from the  $y$  envelopes. The 2D static and dynamic envelopes have shoulders at about  $F = 8.8$  and  $8.6$ , respectively, in Fig. 5(b). They correspond to a sudden appearance of an island [like the one seen e.g. in Fig. 2(b)] in the chaotic attractor and in the snapshot attractor, respectively, at the height of about  $y = 2.5$ , the latter with a decreasing  $F$ . The disappearance of the island occurs via a merging into the mainland and this would not yield a shoulder in the envelope. For increasing  $F$ , as no isolated island from a mainland emerges, no other shoulders can be seen in the dynamic envelope. The difference between the clearly distinguishable shoulders suggest that the dynamic envelope is related to the static one with a *delay* in  $F$ , which is about  $\Delta F = 0.2$  around  $F = 8.8$ .

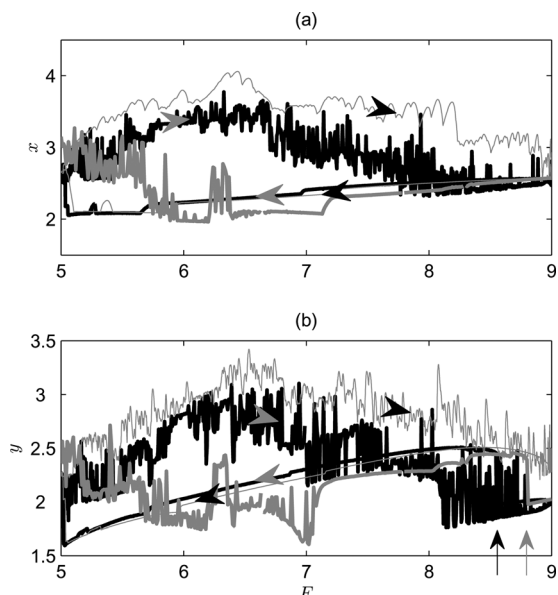


FIG. 5. Dynamic and static envelopes describing extrema in the  $x$  (a) and  $y$  (b) directions. Thin gray line: dynamic envelopes of the 3D snapshot attractor; thick black line: dynamic envelopes on the Poincaré surface  $z=0$  (2D snapshot attractor, same simulation parameters as for Fig. 2). The difference for increasing/decreasing  $F$  indicates in both cases a hysteresis. Thick gray line: static envelopes of the attractors and chaotic saddles of the undriven system at  $z=0$ . Arrowheads placed on branches of the envelopes indicate the direction along the hysteresis loop; for better visibility, the colors of the arrowheads are the reverse of the colors of the envelopes that they belong to. Color-matching vertical arrows point to shoulders of the envelopes.

Based on these observations, the following simplified model helps understand the existence of a hysteresis. Consider a short range of  $F$  where the static envelope is a straight line with some slope. Assume that the height of the dynamic envelope is simply the height of the static envelope taken by  $\Delta F > 0$  earlier (later) when moving towards larger (smaller) values of  $F$ . Thus, two branches of the dynamic envelope arise, as Fig. 7 illustrates. It is also clear from this figure that the sign of circulation around the loop depends on the slope of the static envelope: the circulation is positive for a negative slope.

The real hysteresis is much more complicated than what follows from this simple model. The basic features are the following. (1) The delay in  $F$  is time-dependent. Assuming a fixed temporal delay  $\tau$ , the delay  $\Delta F$  following from Eq. (1) is not constant, but rather it depends on  $t$ , i.e., on the phase of the driving. For relatively small finite values of  $\tau$  the (non-zero) minimum values of  $\Delta F$  will be near the maximal and minimal driving amplitudes,  $F = F_0 \pm A$ . (2) Also the temporal delay  $\tau$  can depend on the dynamical regime passed by, and, thus, on the phase of forcing. (3) A further complication is that the memory of the system cannot be characterized simply by a phase-dependent temporal delay  $\tau$ , but rather an *integral* over the recent past.

The presence of driving prevents transiently chaotic trajectories to reach their periodic or chaotic attractor of the undriven case, as by the time they might come close to such an attractor along the saddle's unstable manifold, this object is already altered.<sup>28</sup> Thus, the hysteresis *cannot be derived* from the undriven case.

The full hysteresis loop is thus much more complex than that of Fig. 7. The origin of it is the temporal delay or memory, and can therefore be called a *memory hysteresis*. Such a hysteresis has been found recently<sup>18</sup> in a global circulation model, e.g., in the diagram of the mean surface temperature and the CO<sub>2</sub> concentration when the latter is increased and decreased periodically at a given rate. In fact, Fig. 3 of Ref. 18 is similar to our Fig. 5. Note, however, that the hysteresis found here is not in thermodynamical averages, but rather in extreme values. This implies that the extremal values of a given variable depend not only on the actual value of the insolation but also on the sign of its temporal change.

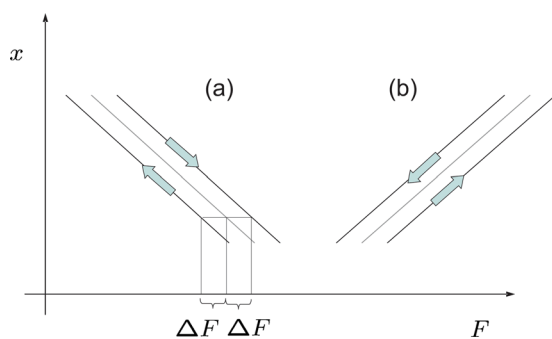


FIG. 7. Schematic diagram illustrating the existence of a hysteresis in a simple model when the dynamic envelope arises as a delayed version of the static one with a positive (negative) delay of magnitude  $\Delta F$  for increasing (decreasing)  $F$ . The slope of the static envelope is negative in case (a) and positive in case (b).

The existence of the hysteresis loop can also be argued on general grounds. The geometry of a snapshot attractor is determined by the history of driving. The influence of the past is gradually declining, that is, the snapshot attractor is determined by the most recent past. When the driving is periodic, two snapshot attractors that belong to the same instantaneous value of the driving, but with opposite signs of change have different histories, and therefore they are expected to have different geometries. The difference should be the largest in the middle of the parameter range of driving, and gradually vanishing towards its minimum and maximum values. Such behavior has been confirmed in a Hénon-type map:  $(x_{n+1}, y_{n+1}) = (d + ax_n^2/(1 + x_n) + y_n, bx_n)$ , with  $a = 3$ ,  $b = 1/2$ , and  $d \in [0.7, 1.1]$ , shifted with an increment  $\Delta d = 0.05$  in a to-and-fro periodic manner. Given that snapshot attractors have a memory, hysteresis is expected to occur very generally in periodically driven systems.

## B. Peak-over-threshold analysis of extreme events

For practical purposes, besides the maximal extreme values, the likelihood of certain extreme events, e.g., peak-over-threshold events, is also sought for. For example, an extreme event can be that the model cyclonic activity is greater than a magnitude of 1.8, that is,

$$r = \sqrt{y^2 + z^2} > 1.8. \quad (2)$$

Fig. 2 illustrates that on the  $z=0$  plane, the line  $y=1.8$  is always close to the upper edge of the attractor, and events beyond this line are rare indeed. In dynamical systems terms, the likelihood of events is seen as a measure of certain parts of the snapshot attractor. In our example, this is  $\mu(r > 1.8)$ . Due to driving, the measure depends on time. With the use of an ensemble, which is followed in 3D, the measure is approximated by the proportion of points in the ensemble that satisfy condition (2). A time series of this measure, that is the likelihood of extremes, is shown in Fig. 8, whose pattern repeats itself—like the driving—annually. Threshold excesses of the time series indicate momentarily likely extreme events. Values of 25 percent might even occur,

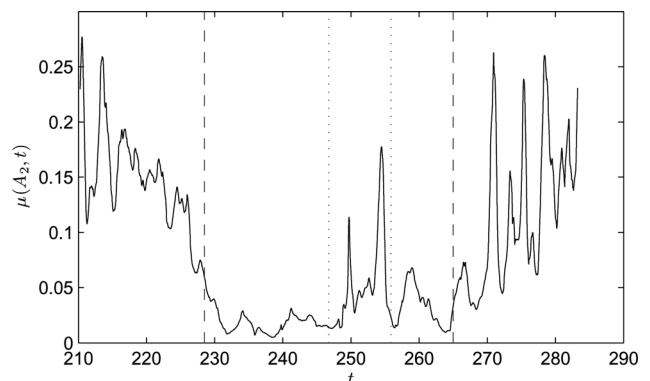


FIG. 8. Time series of the likelihood of extreme cyclonic activities,  $\mu(A_2 = 2, t)$  as defined by condition (2).  $N = 10^6$  points represent the evolving 3D snapshot attractor. The simulation is started at  $t=0$ , and a period of one year is shown, from midwinter to midwinter, after a long time period is discarded.

which are due to the appearances of rather densely populated parts of the snapshot attractor in the regime  $r > 1.8$ .

The return times of likelihoods exceeding a certain threshold, i.e., peak-over-threshold events, is practical and also insightful to consider. It is certainly expected that return times grow with elevated threshold, which is confirmed by the diagram in Fig. 9. In this diagram, several other types of events are also considered, like

$$x < 0, x < 0.5, x > 1.6, \text{ and } x > 1.8. \quad (3)$$

A roughly exponential scaling prevails in limited ranges of threshold values, in agreement with the boundedness of the time series (Fig. 8). The average exponent of scaling ( $\approx 13.8$ ) appears to be basically independent of the particular type of extreme event considered, suggesting that it is a global property in connection with a global structure in phase space.

### VI. CLIMATE SENSITIVITY

It is interesting to investigate this conceptual climate model at another driving amplitude, and to compare the results with those of the previous one, gaining an insight this way into climate sensitivity.<sup>29,30</sup> We change the driving amplitude from  $A = 2$  to  $A = 1$ , by keeping all other parameters fixed. Since  $F_0 = 7$ , the lower turning point at  $F = 6$  does not reach the small- $F$  chaotic regime extending only up to  $F \approx 5.2$ , and points can thus continue coming closer to the periodic attractors of the undriven case until winter sets in again. This process is reflected by the shape of the snapshot attractors (Fig. 10). Before winter, the snapshot attractor is hardly a fractal indicating the near completion of the decay process towards periodic orbits (a). Then, the chaotic winter fattens up the fractal (b), which sees it through the March equinox (c), but by the end of summer, the attractor is almost regular again (d).

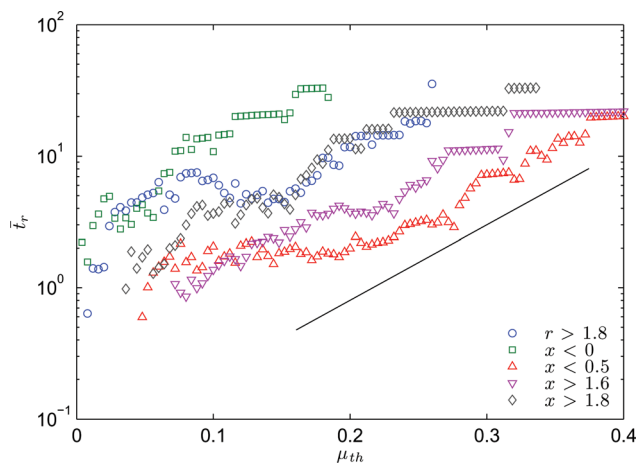


FIG. 9. Mean return times  $\bar{t}_r$  versus varying threshold of peak-over-threshold type extremes in the likelihood of extreme events, as defined by conditions (2) and (3). All of the considered time series are periodic; nevertheless, because of the nontrivial behavior within a period, the scaling may be approximately exponential over limited ranges of the threshold. A solid straight line of slope 13.8 can be fitted to all of the curves over various short ranges of the threshold.

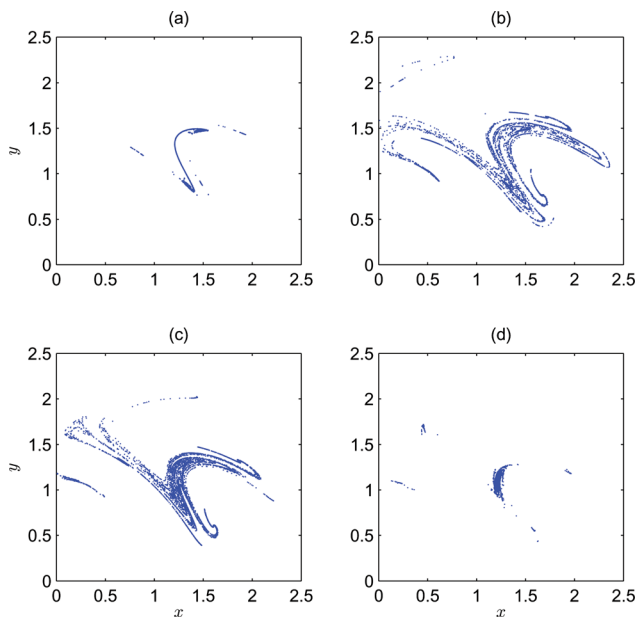


FIG. 10. Snapshot attractors with a reduced driving amplitude  $A = 1$ , at chosen times of the year, associated with (a)  $t = T/12, F(t) = 7.5$ , (b)  $t = 5T/12, F(t) = 7.5$ , (c)  $t = 7T/12, F(t) = 6.5$ , and (d)  $t = 11T/12, F(t) = 6.5$  (enhanced online). [URL: <http://dx.doi.org/10.1063/1.3697984.2>]

The dynamic envelope of extremes also reflects this in Fig. 11. A loop of hysteresis is present again, with a strong decline of the envelope curves for increasing  $F$ . Note that the sign of circulation in the loop here is the opposite to that of Fig. 5.

The likelihood of extreme events of type (2) as shown in Fig. 12 also indicates strong differences. Half the year centered around midsummer, the likelihood almost vanishes. It is remarkable, however, that the largest peak overall with  $A = 1$  might be as large as the one with  $A = 2$ .

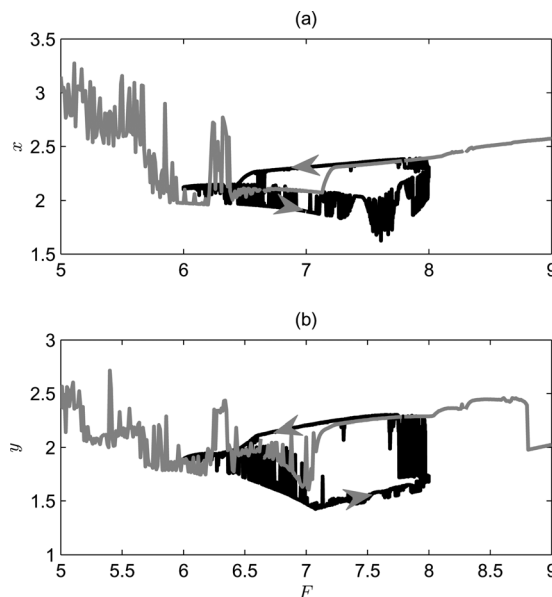


FIG. 11. Dynamic and static envelopes of 2D snapshot attractors (similar to that in Fig. 5) for  $z = 0$ , with a reduced driving amplitude  $A = 1$ . Thick black line: dynamic envelopes and thick gray line: static envelopes. Arrowheads placed onto branches of the envelopes indicate the direction of circulation; for better visibility, the colors of the arrowheads are the reverse of the colors of the envelopes that they belong to.

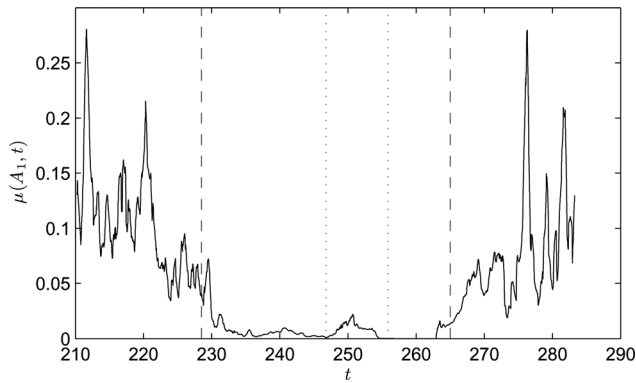


FIG. 12. Time series of the likelihood of extreme cyclonic activities,  $\mu(A_1 = 1, t)$  as defined by condition (2), at  $A = 1$ .

The character of the return time statistics (Fig. 13) hardly changes by reducing the amplitude. In particular, the exponential scaling is characterized by the same exponent, in agreement with the conjecture that it is determined by similar fractal objects in phase space.

A more detailed description of sensitivity can be given by considering time-dependent extreme value properties. In this section, we select one of the different definitions of extreme events (2) and (3) and use condition  $x > 1.8$  throughout. The measure  $\mu(t) \equiv \mu(x > 1.8, t)$  corresponds to the likelihood of finding extremal wind speeds of the Westerlies in L84 as a function of time. Fig. 14 shows the difference in  $\mu(t)$ , i.e.,  $\Delta\mu$ , between  $A_2 = 2$  and  $A_1 = 1$ , which reveals large differences also in wintertime. The peaks of  $\Delta\mu$  indicate climate sensitivity to changes of the amplitude of the annual insolation cycle.

In general, considering any physical observable  $Q \neq 0$  of the climate model, its sensitivity to a change in parameter  $A$  can also be expressed by means of the generalized susceptibility

$$\chi = \frac{1}{Q(A_1)} \frac{\Delta Q}{\Delta A}, \quad (4)$$

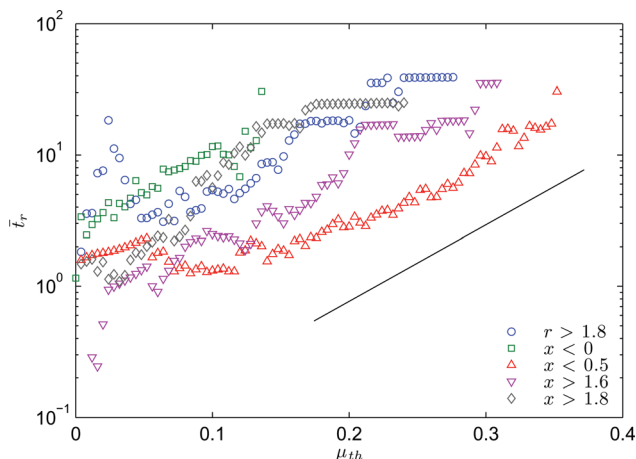


FIG. 13. Mean return times  $\bar{t}_r$  versus varying threshold of peak-over-threshold type extremes in the likelihood of extreme events, as defined by conditions (2) and (3), with  $A = 1$ . The solid straight line has slope 13.8, as in Fig. 9.

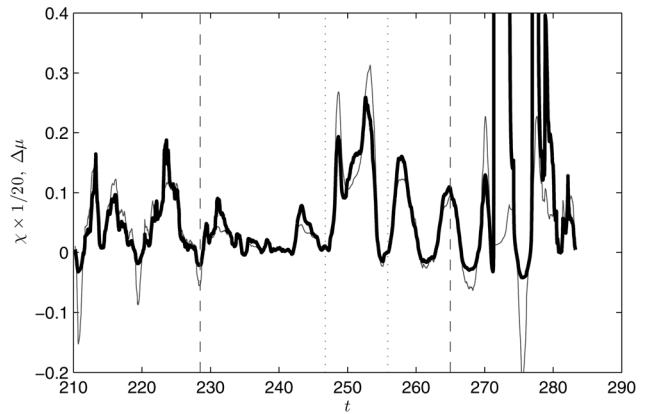


FIG. 14. The difference  $\Delta\mu = \mu(A_2 = 2, t) - \mu(A_1 = 1, t)$  of time series similar to those seen in Figs. 8 and 12 but now for  $\mu(x > 1.8, t)$  (thin gray line). Dividing this by  $\mu(A_1, t)$  results in the time-dependent susceptibility  $\chi(t)$  (thick black line). In a range around  $t = 273$ , the value of  $\chi$  is larger than 8.

where  $\Delta A = A_2 - A_1$  and  $\Delta Q = Q(A_2) - Q(A_1)$ . This quantity can be considered as a function of (dimensionless) time,  $\chi = \chi(t)$ , or also as a quantity based on an average. In this latter case,  $Q$  is replaced by its average,  $\bar{Q}$ , taken over the full year or over different seasons.

The time-continuous version  $\chi(t)$ , with  $Q$  taken as the measure  $\mu(x > 1.8)$ ,  $A_2 = 2$ , and  $A_1 = 1$ , is also shown in Fig. 14. Particular values of  $\chi_{mean}$  for the annual, winter, and summer periods are evaluated, and the results are summarized in Table I. Another, shorter period  $247 < t < 256$  is also considered, in which the largest sensitivity is expected, bracketed by dotted vertical lines in Figs. 8, 12, 14. Winter is taken here as the interval between the September and March equinoxes and summer as the complement interval, bracketed by dashed vertical lines in the same figures.

It should be emphasized that  $\chi_{mean}$  is not the mean of  $\chi(t)$ . Also, the measure of  $\chi(t)$  can be misleading with occasionally small values of  $Q(A_1, t)$ . In fact,  $\mu(A_1, t)$  nearly vanishes for a finite period of time at about  $t = 273$ , and the range of the diagram is set so that corresponding exceedingly large values of  $\chi(t)$  are not featured in Fig. 14. The mere difference  $\Delta\mu = \mu(A_2, t) - \mu(A_1, t)$  is also included in Fig. 14, which gives an absolute measure of sensitivity.

In Table I, all differences and so susceptibilities are positive, i.e., the extremes become more frequent with increasing insolation amplitude; although the time-dependent difference or susceptibility can also be negative (see Fig. 14). Sensitivities are the largest in the distinguished short period indeed. It is remarkable that summers are more sensitive than winters.

A susceptibility of the variance of quantity  $Q$  taken over some period is obtained in a similar fashion as

TABLE I. Susceptibilities (differences  $\times 20$ ), for the mean and variance of variable  $\mu(x > 1.8)$ , evaluated over different time intervals, with a change of amplitude from  $A = 1$  to 2.

Interval	Annual	Winter	Summer	Short period
$\chi_{mean} (\Delta\bar{Q})$	0.69 (0.93)	0.50 (0.80)	0.97 (1.05)	2.00 (2.56)
$\chi_{var} (\Delta\sigma)$	0.56 (0.47)	0.01 (0.01)	3.13 (1.12)	5.34 (1.64)

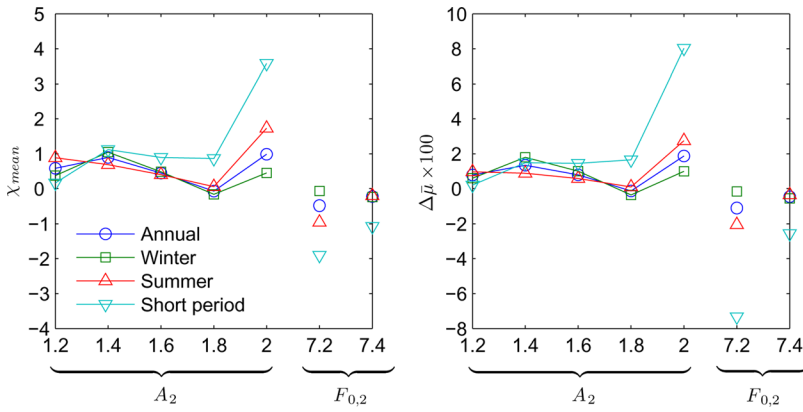


FIG. 15. Susceptibilities  $\chi_{mean}$  (left) taken over periods distinguished by different markers and differences  $\Delta\bar{\mu}$  (right). Parameters  $A$  and  $F_0$  are incremented by 0.2. The horizontal axis labels indicate values,  $A_2, F_{0,2}$ , to which the parameter is increased from values,  $A_1, F_{0,1}$ , smaller by 0.2.  $F_0 = 7$  when  $A_2$  is varied between 1.2 and 2;  $A = 2$  when  $F_{0,2}$  takes on the values 7.2 and 7.4. Markers are connected to guide the eye in reading the  $A_2$ -dependence.

$$\chi_{var} = \frac{1}{\sigma(A_1)} \frac{\Delta\sigma}{\Delta A}, \quad (5)$$

where  $\sigma(A) = (\bar{Q}^2(A) - \bar{Q}(A)^2)^{1/2}$  and  $\Delta\sigma = \sigma(A_2) - \sigma(A_1)$ . With  $Q = \mu(x > 1.8)$  (and  $A_1 = 1, A_2 = 2$ ), annual, winter, summer, and short term variance susceptibilities are given in the second line of Table I. They show that there is a strong increase in the summer variance, but hardly any change in the winter variance.

The common definition of climate sensitivity is based on the doubling of the, say, preindustrial CO<sub>2</sub> content of the atmosphere.<sup>29</sup> Increasing the amplitude  $A$  of insolation, as done above, is not in line with this definition. Instead,  $F_0$  is more appropriate to be increased. Also, the increase of  $A$  from 1 to 2 might be too large of a change. In order to cater for these two points, we examined sensitivity by changing  $A$  and  $F_0$ , both, by smaller positive increments of  $\Delta A = A_2 - A_1 = \Delta F = F_{0,2} - F_{0,1} = 0.2$ . The results of this are presented in Fig. 15. We find that the sensitivity is the strongest in a particular period of the summer, as indicated previously. The sensitivities are found to remain practically constant over an interval  $1.2 < A_2 < 1.8, F_0 = 7$ . For  $A_2 = 2, F_0 = 7$ , and  $F_{0,2} = 7.2, A = 2$ , however, there is a sudden increase in modulus. This can qualitatively be explained by the fact that the driving in these cases enters a range of permanent chaos existing for  $F < 5.2$ , after passing through a long regular regime ( $5.2 < F < 6.6$ ) with transiently chaotic behavior. The regime  $F < 5.2$  is not yet reached at the other parameters (cf. Fig. 3).

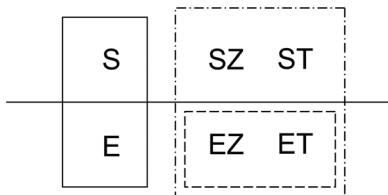


FIG. 16. Classification of numerical sectioning techniques, indicated by boxes drawn using different line styles. (For the explanation of code names, see main text.) Solid: undriven system (single letter codes). Dash dot: techniques applicable to periodic driving. Long dash: techniques applicable to any driving including periodic and aperiodic ones. Horizontal line separates code names of techniques that use either a single long trajectory (S) or an ensemble of trajectories (E).

### VII. CONCLUSIONS

We have investigated the effect of periodic driving on a conceptual climate model. In spite of the temporal simplicity of the driving, 2D snapshot attractors proved to be useful representations of the dynamics and show fractal features throughout the annual cycle, which owes to the fact that transient chaos and chaotic saddles are ubiquitous in the considered parameter regimes.

The effect of fast chaotic driving in the same model has been studied in Ref. 14. Interestingly, the shape of the snapshot attractors with fast chaotic and annually periodic driving was found to be very similar. The abundance of extreme events is also a common feature in the two cases, and more quantitatively, the statistical properties are similar as well. In particular, for the likelihood of extremes, a peak-over-threshold analysis exhibits an approximately exponential increase of mean return times for a limited range of threshold values, although the scaling is less clear in the periodic case.

As a new feature, the model exhibits a hysteresis loop in the extreme values. This is the consequence of an internal memory of the dynamics, suggesting that care must be taken in dealing with the response of climatic extremes. Such events might not only depend on the actual driving strength but also on the history.

To characterize climate sensitivity, we worked out susceptibilities both for the measures of certain extremal events and also for their variance. Evaluating them with temporal averages in different intervals provides new insight into the dynamics of extremes. Although winters are more chaotic in the model, summer susceptibilities are found to be much larger both for averages and variances.

Because of the simplicity of the model, one cannot expect that the numerical value should be in agreement with climatic data. We hope, however, that our qualitative results point to a direction for future research to do with general circulation models.

### ACKNOWLEDGMENTS

Useful discussions with J. Bröcker, K. Fraedrich, I. M. Jánosi, and G. Károlyi are acknowledged. T.B. is grateful for a postdoctoral fellowship given by the Max Planck Society and T.T. for support from the Alexander von Humboldt Foundation. This work was supported by the Hungarian Science Foundation under Grant Nos. OTKA NK72037 and

NK100296. The project is also supported by the European Union and is co-financed by the European Social Fund (Grant Agreement No. TAMOP 4.2.1./B-09/KMR-2010-0003).

## APPENDIX: SECTIONING TECHNIQUES TO CREATE SNAPSHOT ATTRACTORS

Snapshot attractors of driven three-variable systems can be constructed numerically in various ways under different conditions. Techniques may be distinguished according to whether: the system is driven periodically or aperiodically; a single long trajectory or an ensemble of trajectories is used. Here, we provide definitions and details of a few techniques, each of which is coded by letters. For comparison undriven systems are also included, in which case snapshot attractors coincide with traditional attractors. A block diagram of classification is also provided in Fig. 16 for the applied techniques.

**S:** Intersections of a single long trajectory of an undriven system with a surface, called a Poincaré surface of intersection, are taken (a standard and simple technique).

**E:** An ensemble of trajectories of an undriven system are followed mapping subsequent points of intersection with the Poincaré surface. Since the return times of the trajectories to the surface may be different, the ensemble is viewed at discrete “times”—iteratively. Due to ergodicity, **E** results in the same attractor as **S**.

**EZ:** An ensemble of trajectories subject to general driving is followed in the 3D space. After some transient, at any chosen time instant the Poincaré section of the 3D snapshot attractor can be simply approximated by retaining trajectories only whose endpoints stay within a “thick slice” given by a finite  $\delta z$  tolerance around the sectioning surface. Using a finite number of trajectories, however, the measure on the Poincaré surface is not faithfully reproduced numerically, due to the varying “speed” with which trajectories cross the surface.

**ET:** The times and coordinates of crossing are exactly determined by means of interpolation onto the sectioning surface, and those trajectories are selected to represent a snapshot attractor whose crossing time fall in a particular  $\delta t$  short window of time. This way we avoid the numerical problems of **EZ**.

**SZ:** If the driving is periodic, instead of an ensemble, snapshot attractors can be constructed by a single long trajectory too. The trajectory is viewed stroboscopically, and a thick slice with a finite tolerance  $\delta z$  can be taken. First, this suffers from the same problem as **EZ**. Second, with longer period of the driving, a proportionally longer simulation is needed to construct a snapshot which is constituted by the same number of points. Third, if the stroboscopic condition is imposed before sectioning, the stored data from one long simulation is not suitable to represent snapshots at any other phase of the driving, which would be necessary for creating a movie reviewing a complete period (like those of the movies to Figs. 2 and 10).

**ST:** The said drawbacks of **SZ** can be overcome by first sectioning the trajectory by, e.g.,  $z=0$  on the fly in the process of a long simulation, and then from the stored

$(x, y)$  intersection coordinates and crossing time data snapshot attractors can be constructed corresponding to any phase of the driving. To do this, a short window of time of length  $\delta t$  is considered, centered around the chosen phase of the period, and those data points are retained to form a snapshot for which the crossing times  $t \bmod T$  fall into this window of time. As for a movie which shows the time-dependence of the snapshots, a sequence of consecutive phases are considered. Snapshots in different windows are constituted generally by different numbers of points. Another algorithm which produces slightly different snapshots is much more inexpensive, however. When a large number of points is supposed to constitute a snapshot by the above described technique, it is convenient to retain groups of a fixed number, say,  $N = 10^4$  points instead. As for a sequence of  $n$  snapshots, the data points,  $(x_i, y_i)$ ,  $i = 1, \dots, nN$ , are ordered according to the crossing times  $t_i \bmod T$ , and then they are assigned to groups,  $j = 1, \dots, n$ , such that the integer parts of  $i/N$  equal  $j$ . With this, the sizes of the associated windows of time are different. For optimal numerical performance, several long trajectories might have to be considered.

Snapshots from the resulting movie using technique **ST** can be seen in Fig. 2. It has been visually checked that results with **ST** and **ET** indeed agree.

<sup>1</sup>F. Romeiras, C. Grebogi, and E. Ott, *Phys. Rev. A* **41**, 784 (1990).

<sup>2</sup>L. Arnold, *Random Dynamical Systems* (Springer-Verlag, Berlin, 1998).

<sup>3</sup>M. Ghil, M. D. Chekroun, and E. Simonnet, *Physica D* **327**, 2111 (2008).

<sup>4</sup>M. D. Chekroun, E. Simonnet, and M. Ghil, *Physica D* **240**, 1685 (2011).

<sup>5</sup>E. N. Lorenz, *Tellus A* **36A**, 98 (1984).

<sup>6</sup>E. N. Lorenz, *Tellus A* **42A**, 378 (1990).

<sup>7</sup>R. Pielke and X. Zheng, *J. Atmos. Sci.* **51**, 155 (1994).

<sup>8</sup>P. J. Roebber, *Tellus A* **47**, 473 (1995).

<sup>9</sup>A. Shil'nikov, G. Nicolis, and C. Nicolis, *Int. J. Bifurcation Chaos* **5**, 1701 (1995).

<sup>10</sup>A. Provenzale and N. J. Balmford, “Woods hole lecture notes,” available at: <http://www.whoj.edu/fileserver.do?id=21476&pt=10&p=17353> (1999).

<sup>11</sup>A. Leonardo, “Numerical studies on the Lorenz-84 atmosphere model,” M.S. thesis (State University of Utrecht, 2005).

<sup>12</sup>T. Tél and M. Gruiz, *Chaotic Dynamics* (Cambridge University Press, New York, 2006).

<sup>13</sup>J. G. Freire, C. Bonatto, C. C. DaCamara, and J. A. C. Gallas, *Chaos* **18**, 033121 (2008).

<sup>14</sup>T. Bódai, G. Károlyi, and T. Tél, *Nonlinear Processes Geophys.* **18**, 573 (2011).

<sup>15</sup>R. T. Pierrehumbert, talk given at *SIAM Conference on the Application of Dynamical Systems* (Snowbird, 2011).

<sup>16</sup>C. Nicolis, V. Balakrishnan, and G. Nicolis, *Phys. Rev. Lett.* **97**, 210602 (2006).

<sup>17</sup>C. Nicolis and G. Nicolis, *Phys. Rev. E* **80**, 061119 (2009).

<sup>18</sup>I. Bordi, K. Fraedrich, A. Sutera, and X. Zhu, “Transient response to well-mixed greenhouse gas changes,” *Theor. Appl. Climatol.* (in press).

<sup>19</sup>J. C. Sommerer and E. Ott, *Science* **259**, 335 (1993).

<sup>20</sup>J. Jacobs, E. Ott, T. Antonsen, and J. Yorke, *Physica D* **110**, 1 (1997).

<sup>21</sup>Z. Neufeld and T. Tél, *Phys. Rev. E* **57**, 2832 (1998).

<sup>22</sup>Although the snapshot attractors are fractal throughout the annual cycle, the numerically found fractal dimension is known to exhibit large fluctuations around a constant value predicted by theory.<sup>1,31,32</sup>

<sup>23</sup>Wherever we see red points in the absence of blue/green ones, it is thought that the applied numerical technique fails to find them, because the measure of the stable/unstable manifold in those places is very small.

<sup>24</sup>The blank circles around the attractor points indicate the size of their neighborhood used to define escape. A relatively large size had to be used because the attractors are fairly weakly attracting. This is due to the fact

that only a slightly larger extent of the overall attracting trajectories (a period-1 and a period-4 cycle for  $F=6$ ) lie in the dissipative phase space region,  $x < 1 + a/2$ . The (green) unstable manifold certainly extends to within the blank circles, as they guide trajectories to the attractor points, but this can be seen after very long iterations only.

<sup>25</sup>Y.-C. Lai and T. Tél, *Transient Chaos* (Springer, New York, 2011).

<sup>26</sup>The type of the limit distribution of extreme values is not practical to determine, because for a sufficient sample size at a certain phase of the year the simulation would have to be run excessively long. Nevertheless, the limit distributions throughout the year are thought to be all well-approximated by Weibull distributions, with different shape parameters.<sup>14</sup> This is consistent with the fact that any physical snapshot attractor of L84 driven periodically has a finite extension, and therefore, there is a finite maximum value that the variable can take.

<sup>27</sup>For the distribution at a particular phase of the year, data points are obtained from a single trajectory of length  $N$  years on the attractor,  $N \gg 1$ . Equivalently, one can consider an ensemble of  $N$  trajectories over one year on the attractor. For the Poincaré sections, as discussed in case of technique **ST** of the Appendix, a tolerance  $\delta t$  around a phase of the year is chosen. The amount of data obtained depends on the tolerance  $\delta t$ . We found

$\delta t = (1 \text{ year} = 73)/2000 = 0.0365$  to be an appropriate choice. The observational times used in our numerics to generate the dynamic envelopes of the 3D and 2D snapshot attractors are  $10^7$  and about  $4.11 \times 10^5$  years, respectively.

<sup>28</sup>Instead of the static envelope, which is the envelope of the chaotic sets (chaotic attractors or saddles), the envelope of the chaotic saddles' unstable manifold and of the chaotic attractors could also be considered. The problem with this second static envelope is that it assumes a more or less uniform population of the unstable manifold which need not be the case in the presence of driving. In addition, of course, the manifolds are also distorted in the driven system. In fact, this envelope cannot be determined a priori, it can only be found a posteriori, in the full knowledge of the driven dynamics.

<sup>29</sup>R. K. Pachauri and A. Reisinger, *Contribution of Working Groups I, II and III to the Fourth Assessment Report of the Intergovernmental Panel on Climate Change* (Intergovernmental Panel on Climate Change, Geneva, 2007).

<sup>30</sup>R. T. Pierrehumbert, *Principles of Planetary Climate* (Cambridge University Press, 2010).

<sup>31</sup>T. Bódai, G. Károlyi, and T. Tél, *Phys. Rev. E* **83**, 046201 (2011).

<sup>32</sup>F. Ledrappier and L.-S. Young, *Commun. Math. Phys.* **117**, 529 (1988).